

# A Neutron Diffraction and Modeling Study of Uniaxial Deformation in Polycrystalline Beryllium

D.W. BROWN, M.A.M. BOURKE, B. CLAUSEN, T.M. HOLDEN, C.N. TOMÉ, and R. VARMA

The deformation of polycrystalline beryllium to strains of  $\pm 0.8$  pct in uniaxial tension and compression was studied by neutron diffraction and modeled using an elasto-plastic self-consistent (EPSC) model. The beryllium response is asymmetric with respect to tension and compression in both the macroscopic behavior, as displayed in the stress/strain curve, and the microscopic lattice response. The EPSC model qualitatively reproduces the lattice strain curves in tension and compression with the assumption of pyramidal slip being active, in addition to prism and basal slip and with the inclusion of thermal residual stresses developed during processing. Although it underpredicts the magnitude of the observed strains, it demonstrates that accounting for residual stresses of thermal origin is crucial for understanding the evolution of lattice strains during uniaxial loading.

## I. INTRODUCTION

METALLIC beryllium has a number of potential engineering applications that could benefit from its strength, low density, and thermomechanical properties. Its elastic stiffness is comparable to steel, with roughly one-fourth of the density. The thermal conductivity of 147 W/m-K is comparable to aluminum (210 W/m-K), and its melting temperature is relatively high, 1551 K, making it attractive for some high-temperature applications. Unfortunately, at room temperature, beryllium has limited ductility that prevents its use in more wide-ranging applications. In the context of this study, beryllium is of fundamental scientific interest, because it has a hexagonal close-packed crystal structure and displays strong anisotropy of plastic deformation while at the same time relatively low elastic anisotropy.

There have been several studies of the polycrystalline deformation of beryllium in uniaxial tension often aimed at enhancing its limited tensile ductility.<sup>[1-7]</sup> In tension, hot-pressed beryllium typically exhibits a sharp yield point phenomenon, with upper and lower yield points between 325 and 275 MPa, respectively, with an elongation of 0.7 to 3 pct depending on the impurities, heat treatment, and grain size.<sup>[2,4,6,7]</sup> This yield phenomenon in beryllium has been attributed to dislocation pinning by iron-bearing precipitates.<sup>[2,3]</sup> However, Murr *et al.* saw little evidence of dislocation pinning and asserted that plastic deformation was dominated by localized slip at the grain boundaries.<sup>[1]</sup>

Relatively few studies of uniaxial compressive deformation of polycrystalline beryllium exist,<sup>[8-11]</sup> and only those in References 10 and 11 concentrated on hot-pressed material. The upper/lower yield point phenomena reported in tension are not observed for hot-pressed beryllium in compression. No detailed microstructural studies of com-

pressive deformation of beryllium were found in the literature.

The elasto-plastic deformation of polycrystalline metals has been modeled using experimentally observed single-crystal deformation mechanisms and elastic constants within the construct of the elasto-plastic self-consistent (EPSC) model originally proposed by Hill<sup>[12]</sup> and first implemented by Hutchinson.<sup>[13]</sup> Recently, EPSC models have been used to calculate crystallographic lattice strains in individual grains, which, upon suitable averaging, may be compared to neutron diffraction measurements. Comparison of the EPSC model with neutron diffraction data as well as with the macroscopic flow curve is a much more stringent test than comparison with macroscopic curves alone. The EPSC and neutron diffraction studies of fcc<sup>[14-19]</sup> and lower symmetry hcp<sup>[20,21]</sup> metals have been completed with varying success. Preliminary neutron diffraction and EPSC studies of compressive deformation of commercially pure beryllium have recently been reported.<sup>[8]</sup>

Intrinsic to the viability of the EPSC model are assumptions concerning the active inelastic deformation mechanisms. At room temperature, the primary slip system operating in *single crystal* beryllium is basal, designated {0002}  $\langle 11\bar{2}0 \rangle$ , where the dislocations move within basal planes in  $\langle 11\bar{2}0 \rangle$  crystal directions.<sup>[6]</sup> The secondary system is prismatic,  $\{10\bar{2}0\} \langle 11\bar{2}0 \rangle$  (consistent with other hexagonal close-packed metals), although its critical resolved shear stress for activation is several times higher than for basal.<sup>[6,22]</sup> The slip direction (or Burger's vector, **b**) for both basal and prismatic lies in the basal plane precluding the possibility of inelastic behavior in the basal direction. Finally, there is pyramidal *c + a* slip,  $\{11\bar{2}2\} \langle 11\bar{2}3 \rangle$ , which does produce plastic deformation with a component in the  $\langle 0002 \rangle$  direction. However, unlike basal and prismatic slip, room-temperature pyramidal slip has not hitherto been reported in single-crystal beryllium of commercial purity.<sup>[23]</sup> However, above 200 °C, pyramidal slip was observed in single crystals when loaded parallel to the basal plane.<sup>[23]</sup> Evidence of pyramidal slip in polycrystalline samples at elevated temperatures has been reported recently.<sup>[24]</sup>

Another physical feature that must be included in the model is the presence of thermal residual stresses

---

D.W. BROWN, M.A.M. BOURKE, C.N. TOMÉ, and R. VARMA, Technical Staff Members, and T.M. HOLDEN, Visiting Professor, are with the Los Alamos National Laboratory, Los Alamos, NM 87545. Contact e-mail: dbrown@lanl.gov B. CLAUSEN, Staff Member, is with the California Institute of Technology.

Manuscript submitted January 21, 2002.

developed during cooling from the processing temperature due to the anisotropic coefficients of thermal expansion (CTE). The crystallographic CTE of beryllium in the  $\langle 100 \rangle$  and  $\langle 0002 \rangle$  directions are  $13.4$  and  $10.9 \times 10^{-6}/^{\circ}\text{C}$ ,<sup>[25]</sup> respectively, with a weighted average of  $12.6 \times 10^{-6}/^{\circ}\text{C}$  for a nontextured aggregate. Thus, on cooling from the pressing temperature, crystallites will tend to contract in the  $\langle 100 \rangle$  direction more than the average, leaving the  $\{10\bar{1}0\}$  and  $\{11\bar{2}0\}$  crystallographic planes in residual tension at room temperature. Correspondingly, the  $\{0002\}$  planes will be in a state of residual compression at room temperature, such that the overall stress in the aggregate is balanced.

In this article, we report time-of-flight (TOF) neutron diffraction and EPSC modeling studies of the deformation of S200-D grade beryllium in tension and compression. The work was motivated by a prior study of residual stresses in beryllium welds in which disparate results were found depending on the selected diffraction plane.<sup>[26]</sup> We believe the disparities are attributable to intergranular strains, which develop due to the plastic and thermal anisotropy of beryllium and initiated this study of uniaxial deformation in an attempt to understand their evolution.

The advantages of TOF neutron diffraction at a pulsed spallation source are twofold. The resolution in TOF is nearly uniform over the entire spectrum and all diffraction peaks are recorded in the detectors at fixed scattering angles. Thus, the lattice spacings, and hence strains, of all grains oriented to satisfy the diffraction condition in a particular sample orientation are obtained simultaneously. The high resolution of the Neutron Powder Diffractometer (NPD) at the Los Alamos Neutron Science Center, coupled with the excellent neutron scattering properties of beryllium, has permitted the simultaneous analysis of twenty (16 independent) distinct peaks. The resulting comprehensive description of the strain response presented on a stereographic projection allows us to discern the systematic grain-scale behavior for the first time. In conjunction with the EPSC model, this has led to insights concerning thermal effects and active slip systems.

## II. SAMPLE PREPARATION

The specified impurities in S200-D grade beryllium in weight percent are as follows:  $<2$  pct BeO, 0.3 pct Fe, 0.2 pct C, 0.12 pct Si, and 0.08 pct Mg. The initial powder was produced by Braun-type mechanical attrition and sieved to particle sizes less than  $44 \mu\text{m}$ . The resulting powder was vacuum hot pressed into billets at  $1100^{\circ}\text{C}$  and slowly cooled to room temperature. The average grain size of the samples was approximately  $15$  to  $25 \mu\text{m}$ . Hot-pressed S200-D beryllium exhibits a weak texture ( $\sim 1.5$  times random) in which the basal poles are offset from the pressing direction by roughly  $35^{\circ}$ .<sup>[27]</sup> Threaded end tensile samples (ASME standard A370) and compressive samples ( $6\text{-mm}$  diameter  $\times$   $15\text{-mm}$  long) were machined from the billets with the loading axis parallel to the pressing direction. A  $50\text{-}\mu\text{m}$ -thick surface layer was chemically etched from the samples to remove surface cracks due to the machining, which can lead to premature failure of the samples in tension.<sup>[28]</sup>

## III. EXPERIMENTAL DETAILS

*In-situ* neutron diffraction measurements were performed on the NDP at the Manuel Lujan Jr. Neutron Scattering Center, LANSCE, Los Alamos National Laboratory. Details of the NPD are published elsewhere<sup>[29]</sup> and only a short description is presented here. A schematic of a tensile sample and the diffraction geometry is shown in Figure 1 with the diffraction plane in the plane of the figure. The NPD accepts a pulsed white beam of neutrons generated through spallation reactions in a tungsten target and moderated by a water moderator at  $283\text{ K}$ . The incident neutron beam impinges on the gage section of the sample and is scattered in all directions. The volumes of the tension and compression samples immersed in the beam were  $\approx 450$  and  $1250\text{ mm}^3$ , respectively. Detector banks are located  $1.5\text{ m}$  from the sample at  $\pm 90^{\circ}$  deg relative to the incident beam. Each detector bank consists of 31 individual  $^3\text{He}$  tubes, which subtend  $11^{\circ}$  deg in the diffraction plane centered at  $90^{\circ}$  deg in  $2\theta$ . Spectra from individual tubes are summed, with corrections applied for differences in diffraction angle and flight path, to provide a single integrated diffraction pattern for each detector bank. The peak width resolution (FWHM) of NPD is approximately  $2.5 \times 10^{-3}$ .

The samples were deformed *in-situ* using a purpose-built load frame with the load axis oriented at  $45^{\circ}$  deg relative to the incident beam in the horizontal plane. Detectors on either side of the specimen, at  $\pm 90^{\circ}$  deg relative to the beam, record data with diffraction vectors parallel ( $\mathbf{Q}_{\parallel}$ ) and perpendicular ( $\mathbf{Q}_{\perp}$ ) to the applied load simultaneously.<sup>[29,30]</sup> The tensile grips incorporated universal joints to ensure uniaxiality of the applied load, whereas the compression samples were deformed between flat hardened steel platens. Measurements were performed under load control, except

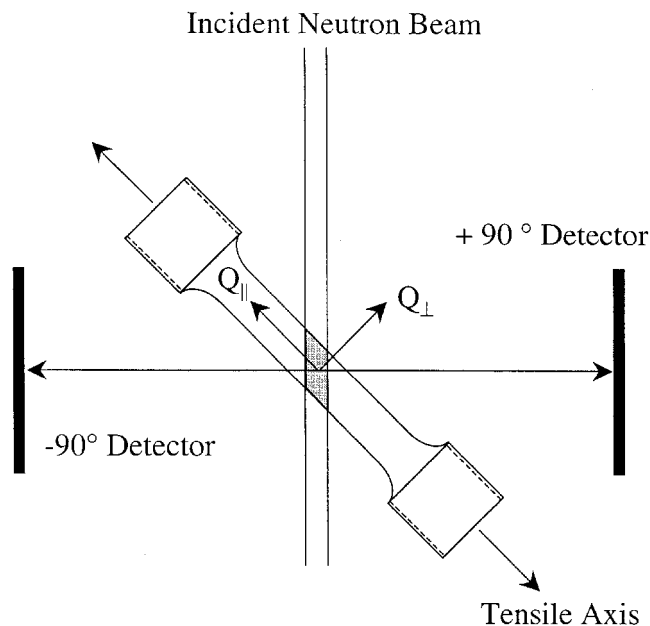


Fig. 1—Schematic of the diffraction geometry showing the scattering vectors  $\mathbf{Q}_{\parallel}$  and  $\mathbf{Q}_{\perp}$  relative to the tensile axis of the sample. Note that the drawing is not to scale.

in the plastic regime of the tensile samples, for which stroke control was used because load control was unstable under zero hardening conditions. The macroscopic strain was determined concurrently with the neutron diffraction measurements using an extensometer that spanned the irradiated region. Measurements of the macroscopic stress/strain curves were also performed *ex-situ*, *i.e.*, without employing the interrupts required for recording the diffraction data. The *ex-situ* and *in-situ* measurements of the flow curve agree satisfactorily.

Two distinct measurement types were employed on separate samples. In the first, the magnitude of the applied stress was increased monotonically with diffraction patterns taken at regular stress intervals to monitor the evolution of the lattice strains in response to the applied stress. The ramp rate between stresses was on the order of 25 MPa/min. with roughly 30-minute hold times during which the diffraction patterns were recorded. In the second, diffraction patterns were recorded after load/unload cycles to incrementally increasing levels of applied stress to monitor the development of the unload residual stresses, which are a signature of the onset of plasticity in the polycrystal.

Interatomic spacings of 16 independent crystallographic planes were determined from the diffraction patterns and the  $(hkl)$  specific lattice strains were calculated from the change in the measured interplanar spacing:

$$\varepsilon_{hkl} = \frac{d_{hkl} - d_{hkl}^0}{d_{hkl}^0} \quad [1]$$

The reference lattice spacing,  $d_{hkl}^0$ , was determined from the measured lattice spacing with a nominal 5 MPa load to hold the sample fixed. As a consequence,  $\varepsilon_{hkl}$  represents a strain change with respect to the hot-pressed and machined state of the sample. Accordingly,  $\varepsilon_{hkl}$  does not account for the thermal residual strains left from sample processing and, thus, should properly be termed “mechanically induced” lattice strain.

#### IV. POLYCRYSTAL MODEL

The EPSC model used in this article is described in detail elsewhere.<sup>[22,30,31]</sup> Briefly, a population of grains is chosen with orientations and weights appropriate for the texture that is to be modeled. After verifying that the weak measured texture of S200-D beryllium had little effect on the calculation, a random texture was assumed for efficiency of computer time. In this case, the random texture was represented by 1000 orientations. Each grain is modeled as a spherical elasto-plastic inclusion embedded in a homogenous effective medium (HEM). The total deformation experienced by a grain depends on its relative stiffness with respect to the HEM that, in turn, is a function of the grain orientation. The elasto-plastic properties of the HEM correspond to the average of all grains and must be solved iteratively. Each grain is defined with appropriate elastic and thermal single-crystal constants. The active slip and twinning systems are defined through their critical resolved shear stress (CRSS) and some hardening behavior. In this work, we have used an extended Voce hardening law characterized by an evo-

lution of the threshold stress with accumulated shear strain in each grain of the form

$$\tau^s = \tau_0^s + (\tau_1^s + \theta_1^s \Gamma) \left( 1 - \exp\left(-\frac{\theta_0^s \Gamma}{\tau_1^s}\right) \right) \quad [2]$$

where  $\Gamma$  is the accumulated shear in the grain,  $\tau_0^s$  is the initial CRSS of system  $s$ ,  $(\tau_0 + \tau_1)$  is the back-extrapolated stress at the origin,  $\theta_0$  is the initial hardening rate, and  $\theta_1$  is the final linear asymptotic slope in the hardening response.<sup>[31]</sup>

For the purposes of the model, it was assumed that the thermal residual stresses began developing at 750 °C on cooling since the yield strength of beryllium is small above this temperature.<sup>[32]</sup> The simulated sample was first cooled from 750 °C to room temperature. Then, it was loaded in tension or compression applied in strain increments of  $10^{-4}$ , to a total strain of 0.8 pct consistent with the experiment. Finally, the sample was unloaded in stress control over 20 steps.

For comparison with the diffraction measurements, subsets of grains were identified from the texture file whose  $(hkl)$  plane normals are oriented to match the diffraction condition defined by the instrument. In practice, grains with normals within an angular range ( $\pm 5$  deg) of the exact diffraction requirement were used, consistent with the angular range of the detectors, which is  $\pm 5.5$  deg ( $2\theta$ ).

## V. EXPERIMENTAL RESULTS

### A. Macroscopic Response

The macroscopic stress/strain curves in tension and compression are shown in Figure 2. The inset shows an enlargement of the elastic-plastic transition with the sign of the data changed so the curves overlap. The macroscopic behavior of

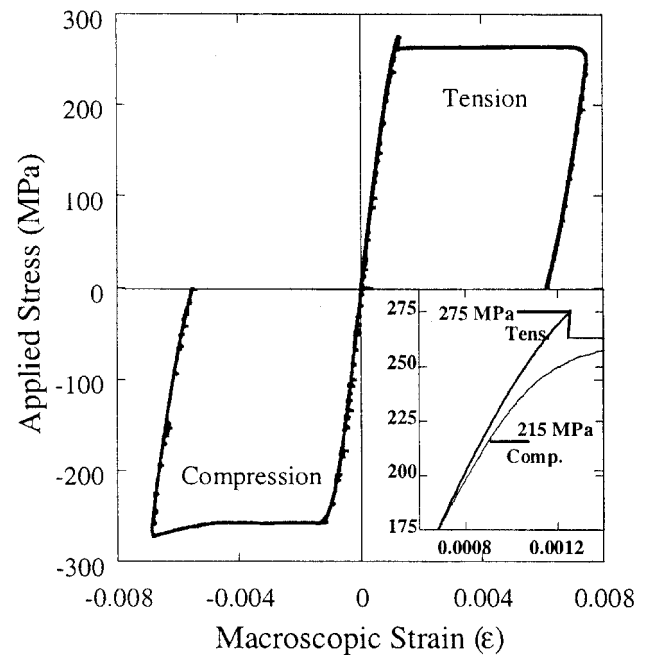


Fig. 2—Macroscopic stress/strain response of S-200D beryllium in tension and compression. The inset shows a blowup of the elastic-plastic transition region of each flow curve.

the samples in tension and compression in the linear elastic, plastic ( $>0.15$  pct strain), and unloading regions is very similar. However, the elastic-plastic transition differs qualitatively between the two cases. The beryllium sample responded nearly linearly to applied tensile stress until roughly 275 MPa, followed by a sharp yield point phenomenon, consistent with previous reports.<sup>[1,2,3]</sup> In contrast, in compression, the strain response departs from linearity at roughly  $-215$  MPa with a smoother elastic-plastic transition. In both tension and compression, once plastic deformation is initiated, the samples deform with essentially no hardening. At higher strains, above  $-0.6$  pct in compression, a small amount of hardening is evident. Also, we observe nonlinear unloading behavior in both tension and compression.

### B. Lattice Plane Response

Figure 3 shows the diffraction pattern recorded in the  $-90$  deg detector bank (diffraction vector parallel to the load) from the beryllium tensile sample at a load of 5 MPa. The inset shows an enlargement of the pattern in the  $d$ -space range of 0.60 to 0.83 Å to highlight the quality of the data. Overall, the strain response of 20 different crystallographic planes, 16 of which were first-order peaks, was tracked during the measurement. To the authors' knowledge, this is the first time such complete coverage of the crystallographic orientations has been achieved during an *in-situ* loading measurement, providing new insight into the deformation behavior of the polycrystal aggregate.

We begin by discussing the observed residual lattice strains measured following load/unload cycles to progressively increasing maximum stress shown in Figure 4. After tensile loading, significant residual stresses develop only after a loading to stresses in excess of 270 MPa, corresponding to the deviation from linearity seen in Figure 2. In contrast, after compressive loading, residual stresses appear after loads of 200 MPa. This indicates that the material deformed plastically earlier than in tension, probably below 200 MPa, again consistent with the macroscopic flow curve shown in Figure 2. Also of significance is the dissimilar behavior of the  $\{hkil\}$  specific residual strains between tension and compression. For example, in Figure 4, the  $\{0002\}$  orientation after tensile and compressive deformation shows residual strains that are strongly tensile and almost zero, respectively. Prediction of this asymmetry provides a strong test for our ability to understand microstructural deformation processes.

The lattice plane specific  $\{hkil\}$  stress/strain curves during monotonic loading were also measured and are shown in Figure 5. Figures 5(a) through (f) show the lattice strain response of the grains with  $\{10\bar{1}0\}$ ,  $\{10\bar{1}1\}$ ,  $\{10\bar{1}2\}$ ,  $\{10\bar{1}3\}$ ,  $\{10\bar{1}4\}$ , and  $\{0002\}$  plane normals parallel to the applied stress direction for both compression and tension. Circles and diamonds represent the strain response in tension and compression, respectively. Open and closed symbols distinguish between load and unload, respectively. The uncertainty in the strain measurement is between 20 and 50  $\mu\epsilon$  depending on the strength of the diffraction peak associated with a given  $\{hkil\}$ .

The expected plane-specific response in the purely elastic regime, calculated from the single-crystal elastic con-

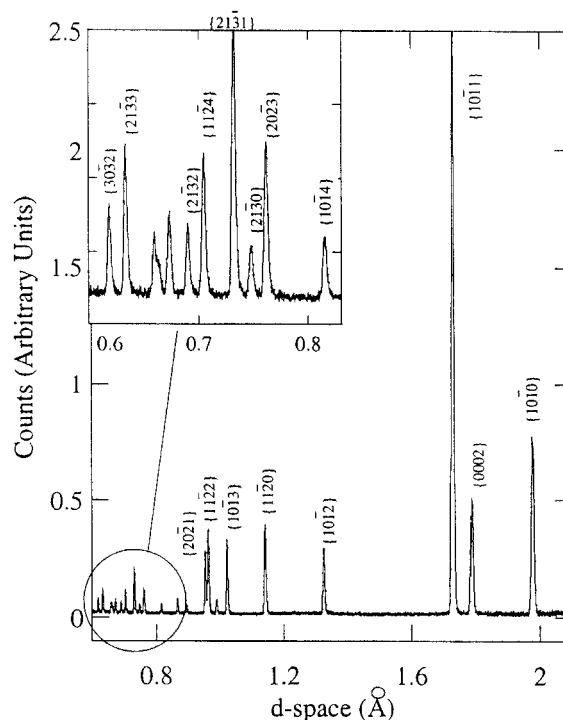


Fig. 3—Diffraction pattern from beryllium at 5 MPa applied stress. The inset shows an enlargement (12.5 times) of the region of the pattern from  $d = 0.6$  to  $0.83$  Å.

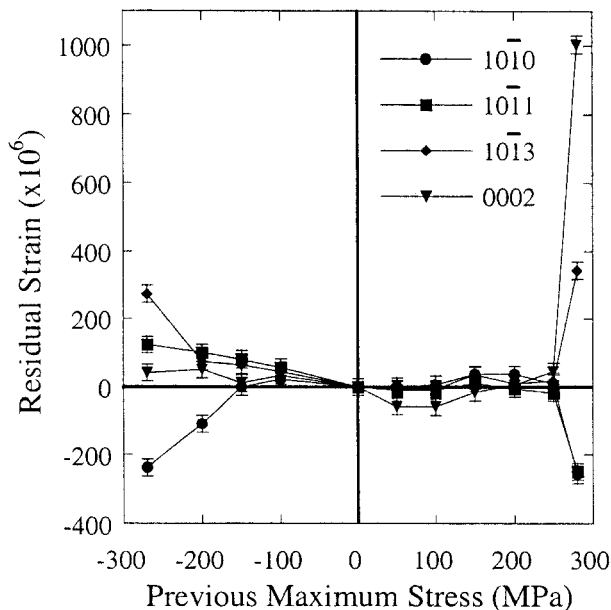


Fig. 4—Residual lattice strains following load-unload cycles to increasing maximum applied stresses in tension and compression.

stants and the texture (random in this case), is indicated by the solid lines passing through the origin for each  $\{hkil\}$ . As in the macroscopic stress/strain curve, deviations from linear elastic behavior are seen in compression at a lower

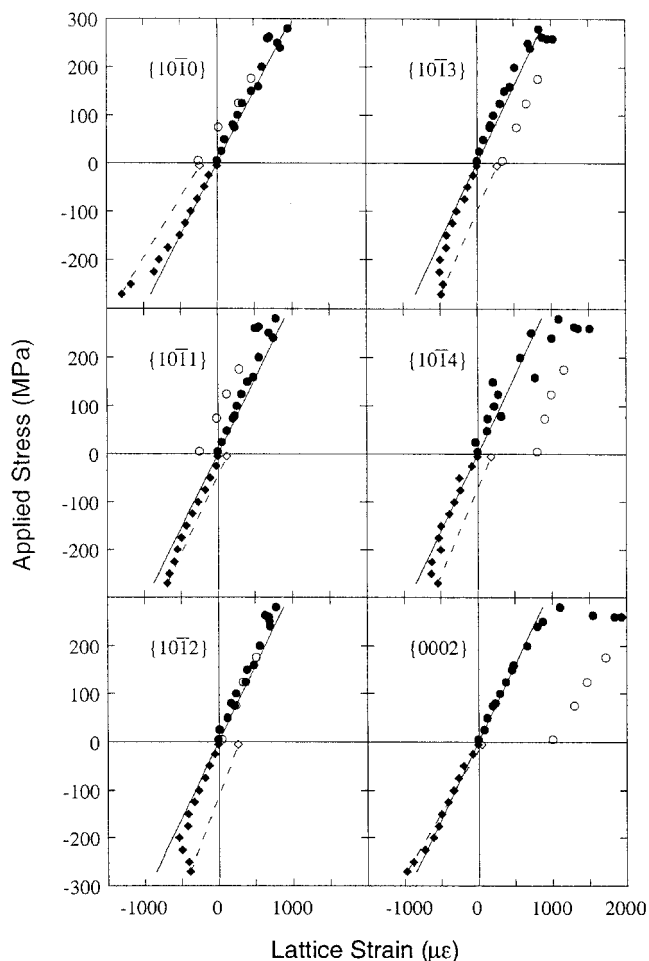


Fig. 5—Lattice strain associated with the  $\{10\bar{1}0\}$ ,  $\{10\bar{1}1\}$ ,  $\{10\bar{1}2\}$ ,  $\{10\bar{1}3\}$ ,  $\{10\bar{1}4\}$ , and  $\{0002\}$  reflections parallel to the applied compression and tension. Closed (open) symbols represent loading (unloading). The dashed lines are guides to the eye.

applied stress than in tension for all individual planes shown. This is a microscopic manifestation of the “early yield” in compression noted in reference to the macroscopic stress/strain curve (Figure 2).

When plastic deformation occurs, the strain response of each crystallographic plane  $\{hkil\}$  no longer follows the line given by the diffraction elastic constant. Departures of the lattice strain (associated with a set of grains with a given orientation) above the calculated elastic line (in an absolute sense) indicate that the grain orientation has yielded (deformed plastically). Conversely, deviations of the  $hkil$ -specific lattice strain below the calculated line indicate that *other* grains in the polycrystalline aggregate have yielded, transferring the load to the remaining orientations. This representation is not strictly accurate in a material with multiple active slip systems, such as beryllium, but may be considered a rule-of-thumb and will be used in the following discussion for descriptive purposes.

To follow the complex loading behavior of the beryllium polycrystalline aggregate, we consider the trends that exist for the  $\{10\bar{1}l\}$  planes with increasing  $l$  approaching the basal pole,  $\{0002\}$ . We begin with a close examination of

the lattice strains measured in grains oriented with the  $\{10\bar{1}0\}$  plane normal parallel to the loading axis. In tension above roughly 275 MPa, the  $\{10\bar{1}0\}$  strain (Figure 5(a)) deviates above the calculated elastic response and acquires a negative residual strain indicating that plastic deformation has occurred in grains with  $\{10\bar{1}0\}$  poles parallel to the loading axis. At an applied stress of roughly  $-200$  MPa in compression, the  $\{10\bar{1}0\}$  departs below the linear response (in an absolute sense) indicating that grains of this orientation have not yielded, but instead are supporting a greater portion of the load as other sets of grains deform. Therefore, we conclude that grains with  $\{10\bar{1}0\}$  plane normals parallel to the loading direction yield in tension, but not in compression.

In tension, the  $\{10\bar{1}1\}$  strain (Figure 5(b)) behaves like the  $\{10\bar{1}0\}$ . Plastic deformation occurs for this grain orientation and the grain acquires a compressive residual strain on unloading. However, the behavior of the  $\{10\bar{1}1\}$  strain under compressive loading differs from the  $\{10\bar{1}0\}$ . The slope of lattice strain vs applied stress is greater than the calculated elastic line indicating that plastic deformation has occurred in these grains in compression as well as in tension.

Focusing again on the  $\{0002\}$  grains in tension, beyond the onset of plasticity, they exhibit strains that are larger than the calculated elastic response (solid lines in Figure 5). This indicates that they support a larger fraction of each stress increment after plasticity and is consistent with load being shed from grains in other orientations that are yielding. This is expected since the resolved shear stress on the two primary active slip systems in beryllium, basal and prismatic, is zero in grains with basal poles parallel to the stress. However, the  $\{0002\}$  strains in compression differ dramatically, remaining near the calculated elastic behavior even as grain orientations, such as the  $\{10\bar{1}2\}$  and  $\{10\bar{1}3\}$ , begin to deform plastically. This indicates that grains with basal poles parallel to the compressive axis must have some mechanism of inelastic deformation. This contrast in behavior between tension and compression is unambiguous and requires an explanation.

A summary of the  $hkil$ -specific residual strains observed for poles in the plane containing the  $\{10\bar{1}0\}$  and  $\{0002\}$  poles, that is plane normals of the form  $\{h0hl\}$  is given in Table I. Also shown in Table I are the angles from the basal pole and  $hkil$ -specific moduli for each orientation. When examined as a whole, moving from the  $\{10\bar{1}0\}$  to the  $\{0002\}$  pole, a definite trend exists in the residual strain, the details of which differ between tension and compression. In tension, the residual strains are constant ( $\sim -250 \mu\epsilon$ ) to within our uncertainty between the  $\{10\bar{1}0\}$  and  $\{10\bar{1}1\}$  poles and subsequently increase monotonically from the  $\{10\bar{1}1\}$  pole to reach a maximum of  $1000 \mu\epsilon$  at the  $\{0002\}$  pole. In contrast, in compression, the residual strains increase from the  $\{10\bar{1}0\}$  pole, reach a maximum near the  $\{10\bar{1}3\}$  pole, and thereafter decrease to nearly zero at the  $\{0002\}$  pole (Figure 5).

The lattice strain response perpendicular to the applied stress for the same subset or orientations is shown in Figures 6(a) through (f) for both compression and tension. The solid lines passing through the origin for each  $\{hkil\}$  indicate the expected Poisson's ratio response in the purely elastic regime. Since the Poisson's ratio of beryllium is

**Table I. Residual Strains as Measured for the  $\{h0\bar{h}l\}$  and  $\{0002\}$  Planes Normals Parallel to the Loading Direction after a Load/Unload Cycle to 0.7 Percent in Tension and  $-0.8$  Percent in Compression, Respectively; Uncertainties are between 25 and 50  $\mu\epsilon$  Depending on the Strength of the Reflection**

Reflection	Angle from Basal Pole (Deg)	$E_{hkil}$ (GPa)	Residual Strain in Tension ( $\mu\epsilon$ )	Residual Strain in Compression ( $\mu\epsilon$ )
$\{10\bar{1}0\}$	90.00	300	-260	-240
$\{20\bar{2}1\}$	74.56	303	-270	-100
$\{10\bar{1}1\}$	61.08	310	-250	-120
$\{20\bar{2}3\}$	50.35	315	30	-170
$\{10\bar{1}2\}$	42.15	319	50	260
$\{10\bar{1}3\}$	31.11	322	340	270
$\{10\bar{1}4\}$	24.35	322	800	180
$\{0002\}$	0	321	1000	40

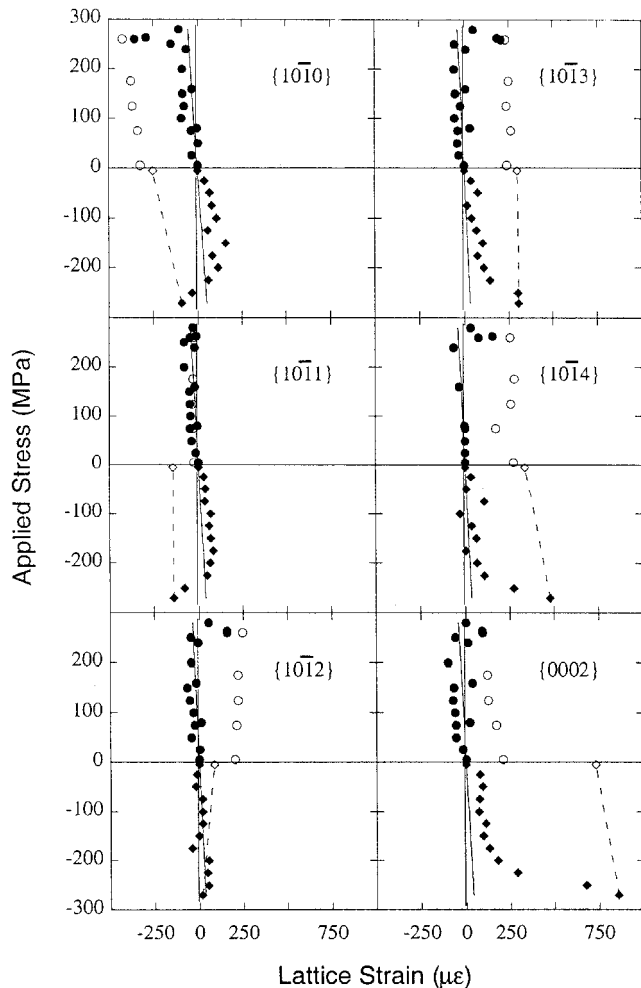


Fig. 6—Lattice strain associated with the  $\{10\bar{1}0\}$ ,  $\{10\bar{1}1\}$ ,  $\{10\bar{1}2\}$ ,  $\{10\bar{1}3\}$ ,  $\{10\bar{1}4\}$ , and  $\{0002\}$  reflections perpendicular to the applied compression and tension. Closed (open) symbols represent loading (unloading). The dashed lines are guides to the eye.

abnormally small ( $\sim 0.04$ ), little elastic response perpendicular to the applied stress is expected. Again, the lattice strains deviate from the linear elastic response in compression at lower stresses than in tension.

## VI. DISCUSSION

### A. Evolution of Intergranular Strains with Plastic Deformation

The measured lattice strains,  $\epsilon_{hkil}$ , parallel and perpendicular to the applied load,  $\sigma$ , recorded during a load test may be expressed as the sum of two components:

$$\epsilon_{hkil} = \frac{\sigma}{E_{hkil}} + \epsilon_{hkil}^I \text{ (parallel) and} \quad [3]$$

$$\epsilon_{hkil} = \frac{V_{hkil}\sigma}{E_{hkil}} + \epsilon_{hkil}^I \text{ (perpendicular)}$$

where the first term represents the response to the macroscopic applied load,  $\sigma$ , and  $\epsilon_{hkil}^I$  the response to intergranular stresses for a given grain orientation ( $hkil$ ). The intergranular strain,  $\epsilon_{hkil}^I$ , arises from the combined effects of elastic anisotropy ( $E_{hkil}$ ), thermal anisotropy ( $\alpha_{hkil}$ ), and plastic anisotropy (associated with different inelastic deformation modes). The elastic anisotropy of beryllium is relatively small compared to the other effects with the plane specific elastic moduli varying by roughly  $\pm 4$  pct from the average (Table I) and are ignored in this study. In the following discussion, we will consider intergranular strains arising due to both thermal and plastic anisotropy. However, we stress that due to our adoption of the initial interplanar spacing as  $d_{hkil}^0$  (Eq. [1]) in our analysis of the neutron diffraction data, the thermal intergranular strains are explicitly ignored and the following plots of the intergranular strains reflect only those originating during plastic deformation.

The plasticity-induced intergranular strains were determined experimentally using Eq. [3] and the  $hkil$ -specific elastic moduli calculated from the single-crystal stiffnesses. Since 16 independent crystallographic planes were measured, the most efficient way to view all of the recorded data is in the form of stereographic projections. Figure 7(a) shows the location of the poles of the analyzed planes on the standard hexagonal close-packed projection. Figures 7(b) and (c) show the contribution to the intergranular strains from plasticity after macroscopic strains of (b)  $-0.8$  pct and (c) 0.7 pct. The measured values are listed in locations consistent with the pole labels shown in Figure 7(a). The experimental uncertainty in the strain measurements is between 25 and

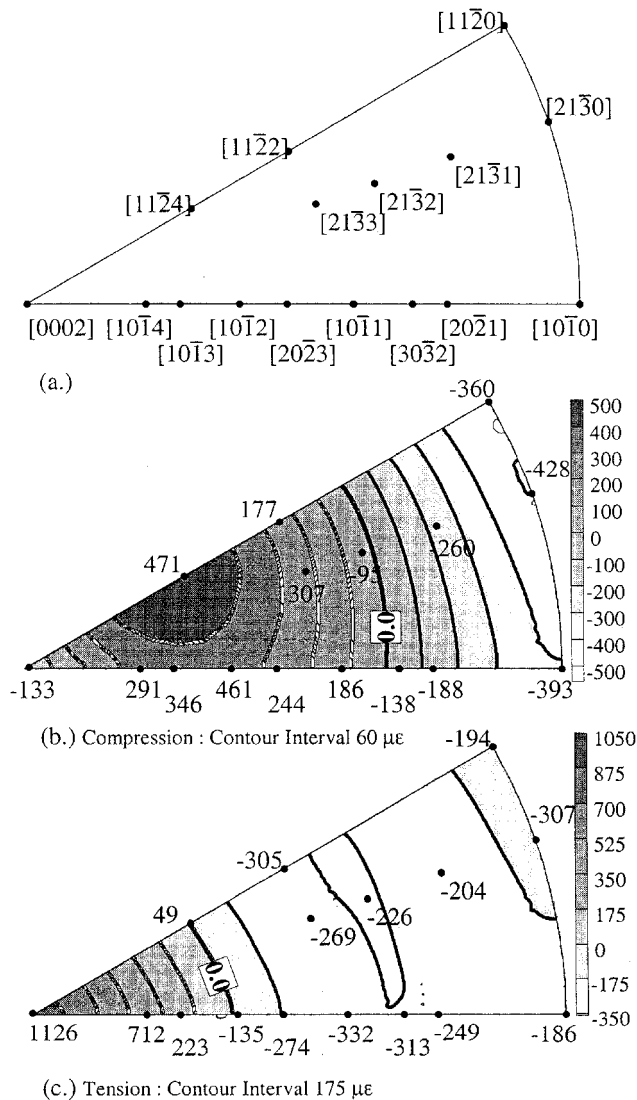


Fig. 7—Experimentally determined plasticity-induced intergranular strains ( $\mu\epsilon$ ) resulting from macroscopic strains of (b)  $-0.8$  pct ( $c = 275$  MPa) and (c)  $0.7$  pct ( $c = 263$  MPa) shown on a stereographic projection. Figure 7(a) indicates the location of the 16 independent crystallographic directions monitored during the experiment. Uncertainties are between  $\pm 25$  and  $\pm 50 \mu\epsilon$  depending on  $hkl$ .

$50 \mu\epsilon$  depending on the intensity of the diffraction peak associated with a given orientation. Although not shown, the intergranular strains develop smoothly as a function of macroscopic strain from zero strain to the extreme values plotted in Figures 7(b) and (c).

The discrete data shown in Figure 7 have been fit to a tensor form

$$\Delta d/d = 1_i 1_j \epsilon_{ij} \quad [4]$$

assuming a single tensor  $\epsilon_{ij}$  with principal axes along the crystallographic directions  $[10\bar{1}0]$ ,  $[\bar{1}2\bar{1}0]$ , and  $[0002]$  for the purpose of drawing the intergranular strain contours on the stereographs. While we have no physical justification for this procedure, it turns out that the data are consistent with this simple assumption and the fits are quite good.

The stereographic projections clearly reveal the systematic variation of the intergranular strains with orientation associated with both tensile and compressive plasticity. In tension (Figure 7(c)), there is a strong variation of the plasticity induced intergranular strain between the  $\{0002\}$  and  $\{10\bar{1}1\}$  poles with a zero between  $\{10\bar{1}2\}$  and  $\{10\bar{1}3\}$ . The zero in the plane containing  $\{0002\}$  and  $\{11\bar{2}0\}$  comes at nearly the same radial distance from the  $\{0002\}$  pole. The variation of the intergranular strain is less dramatic between the  $\{10\bar{1}1\}$  and  $\{10\bar{1}0\}$  poles with a weak minimum apparent at roughly  $70$  to  $75$  deg from the  $\{0002\}$  pole near the  $\{30\bar{3}2\}$  and  $\{21\bar{3}2\}$  poles. In contrast, in compression, the zero of the intergranular strain is near the  $\{30\bar{3}2\}$  and  $\{21\bar{3}2\}$  poles and a maximum is present near  $\{11\bar{2}4\}$  and  $\{10\bar{1}2\}$ , roughly  $40$  deg from the basal pole. The variation of the intergranular strains is consistent with the residual strains described in Table I.

### B. EPSC Model

The difference in tensile and compressive behavior exhibited by the intergranular strains is apparent in Figures 7(b) and (c). To reproduce the observed behavior we included thermal residual stresses, basal prismatic, and pyramidal slip in the model calculation. The lack of compressive residual strain observed for the  $\{0002\}$  in compression indicates that a relaxation mechanism parallel to the basal pole is active in compression. Furthermore, the existence of thermal residual stresses, which are quite plausible, and activity of pyramidal slip are necessary to explain the tension-compression asymmetry.

Specifically, it is necessary to postulate pyramidal slip because the shear stress resolved on the basal and prismatic systems due to the thermal residual stresses (TRS's) is zero. This requirement for pyramidal slip to provide the catalyst for asymmetry is evident by considering the shear stress due to the thermal stress resolved on the  $i$ th slip system,

$$\tau^i = \frac{\sigma_{kl}^{TRS}}{2} (b_k^i n_l^i + b_l^i n_k^i) \quad [5]$$

where  $n^i$  and  $b^i$  are the normal to the slip plane and its slip direction. For a random texture, the thermal residual stress tensor expressed in the crystal coordinate system of the hexagonal structure adopts the form

$$\sigma^{TRS} = \begin{bmatrix} S_{11} & 0 & 0 \\ 0 & S_{11} & 0 \\ 0 & 0 & S_{13} \end{bmatrix} \quad [6]$$

Substitution of the plane normal and slip direction for basal and prismatic slip,  $\{0002\} \langle 10\bar{2}2 \rangle$  and  $\{10\bar{1}0\} \langle 11\bar{2}0 \rangle$ , respectively, results in zero resolved shear stress in each case.

This assumption of pyramidal slip is controversial because it has not been observed in single crystals<sup>[23]</sup> below  $200$  °C. However, the constraints on a single crystal during compressive deformation (transverse surfaces are unconstrained) differ significantly from those on a single grain embedded in a polycrystal. We believe that the difference in boundary conditions between deformation of a single crystal and a single grain within a polycrystalline matrix is sufficient to

consider the possibility of pyramidal in the polycrystalline sample at room temperature.

Other possibilities that may be considered to explain the asymmetry include crystallographic texture, polar CRSS and hardening parameters, grain boundary fracture, and twinning. When we ran the model with and without the reported texture of hot-pressed S200-D grade beryllium,<sup>[27]</sup> the differences in the calculated lattice strains were less than 5 pct. Therefore, the presence of texture proved insufficient to explain the asymmetry. Polar CRSS and hardening parameters are generally considered unphysical. The experimental signature of grain-boundary fracture would likely be apparent in tension only and would not in any simple sense explain the compressive response.

Concerning twinning, transmission electron microscopy (TEM),<sup>[22,33]</sup> and texture<sup>[34]</sup> measurements have demonstrated that beryllium twins on the  $\{10\bar{1}2\}$   $\langle\bar{1}011\rangle$  system when subjected to a compressive stress perpendicular to the basal pole. However, in these references, no twinning was observed when the compression was parallel to the basal pole (precluding the relaxation of  $\{0002\}$  strains parallel to the load in contrast with the behavior that was observed in this study). Furthermore, during the diffraction measurements reported here, no intensity changes were noted that might be associated with twin reorientation.<sup>[35]</sup> (The experimental sensitivity to twinning is typically better than 5 pct volume fraction.)

### C. Thermal Intergranular Strains

Concerning the thermal residual stresses, the explanation used in this article is similar to the explanation of the flow curve asymmetry observed in an annealed Zirconium alloy\*.<sup>[36]</sup>

\*ZIRCALOY is a trademark of . . .

Because the thermal residual strains introduced on cooling from the pressing temperature have not been measured experimentally, the EPSC model was used to calculate them. The calculated TRS's are an upper bound because the model assumes a temperature-independent elastic modulus and yield strength. Figure 8 shows the calculated TRS's for the reflections subsequently monitored in our neutron diffraction study. The calculated TRS's can also be expressed in tensor form by

$$\sigma^{TRS} = \begin{bmatrix} 127 & 0 & -1 \\ 0 & 124 & 0 \\ -1 & 0 & -237 \end{bmatrix} \text{MPa}$$

The minor deviations of the TRS tensor from the format given in Eq. [6] are due to the limited number of grains (1000) used in the calculation.

The magnitude of the calculated TRS's is significant. The thermal residual stress on the prism planes, 127 MPa, is nearly 1/2 of the ultimate tensile strength of the material and biases these planes to yield in tension. Correspondingly, the presence of the thermal residual stresses predisposes orientations having the basal pole aligned with the loading axis to yield prematurely in compression, and to delay yielding in tension. Furthermore, the magnitude of the thermal residual stress is larger in compression in orientations near the

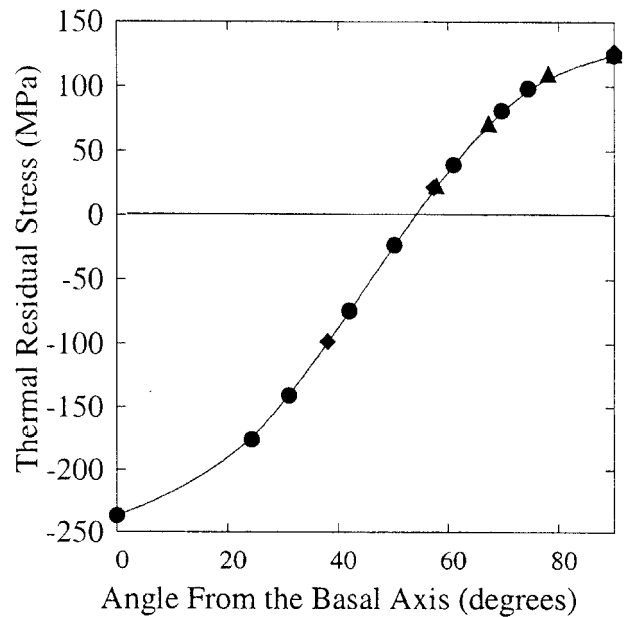


Fig. 8—Calculated thermal intergranular stresses developed in beryllium after cooling from the pressing temperature of 750 °C. The data are plotted as a function of hkl between the basal pole and basal plane at three polar angles about the basal pole. ●'s, ▲'s, and ◆'s represent hkl's within the planes defined by the  $\{0002\}$  and  $\{10\bar{1}2\}$  plane normals, the  $\{0002\}$  and  $\{11\bar{3}0\}$  plane normals, and the  $\{0002\}$  and  $\{12\bar{2}0\}$  plane normals, respectively.

Table II. CRSS's of the Slip Systems Assumed Active in the EPSC Model

Slip System	Designation	$\tau_0$ (CRSS) (MPa)	$\tau_0$ (CRSS) (MPa) in Ref.6
Basal	$\{0002\}\langle 11\bar{2}0\rangle$	30	<10
Prismatic	$\{10\bar{1}0\}\langle 11\bar{2}0\rangle$	140	50
Pyramidal	$\{11\bar{2}2\}\langle 11\bar{2}3\rangle$	325	2000

basal pole relative to the tensile thermal residual stress near the prism pole, suggesting that macroscopic yield will occur at a lower applied stress in compression than tension.

Starting from this state, the macroscopic and lattice specific response to the applied compressive and tensile stresses were calculated. The model assumes that basal, prismatic, and pyramidal ( $c + a$ ) slip modes are active with CRSS's given in Table II. For general comparison, reported CRSS's for single-crystal beryllium are also shown in the table, (6). The hardening parameters were maintained at essentially zero to attempt to reproduce the perfectly plastic response of the material above strains of 0.15 pct. The CRSS's were varied systematically to optimize the agreement between the calculated and observed lattice strains. Agreement between the calculated and observed macroscopic flow curves was considered a secondary goal.

### D. Macroscopic Stress/Strain Curve

Figure 9 shows a comparison of the observed and calculated flow curves in compression and tension. The model captures most of the exhibited behavior in tension and compression, including the prediction of some Bauschinger effect

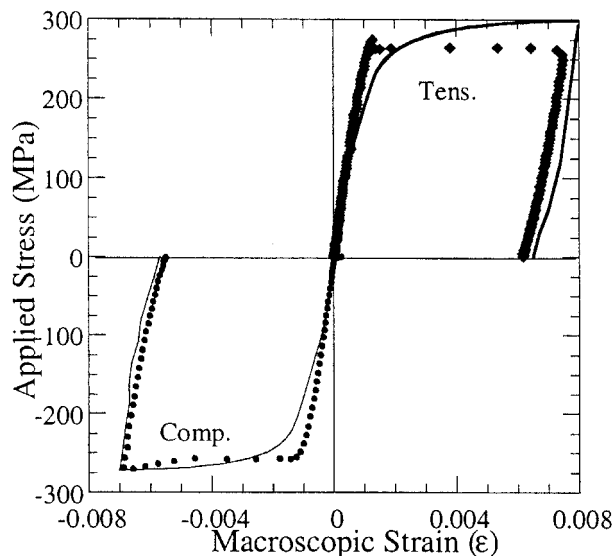


Fig. 9—Experimental (symbols) and calculated (solid lines) macroscopic flow curves of beryllium in tension and compression.

(nonlinear relaxation) during unloading. However, the model predicts an elasto-plastic transition that is much less sharp than the one observed experimentally. The model contains no physical mechanism that can predict the yield point phenomenon observed in tension that is reportedly due to dislocation pinning.<sup>[2,3]</sup> Moreover, in order to optimize the agreement with the lattice strains, CRSS's were chosen that have led to the calculated macroscopic curve departing from linear elastic behavior earlier than is observed. However, it is noted that due to the thermal residual stresses, the model predicts that deviation from linear elastic behavior will occur in compression at stresses 10 to 20 MPa lower than in tension, consistent with the observed macroscopic asymmetry. Also, the model does not predict the late hardening (above  $-0.6$  pct) observed in compression. Only one neutron diffraction pattern was taken after this point so we have no information to elucidate this behavior.

#### E. Elastic Lattice Response

Figure 10 shows the measured and modeled lattice response in grains with  $\{10\bar{1}0\}$  and  $\{0002\}$  plane normals parallel and perpendicular to the applied stress in compression and tension. The agreement between the experiment and model is qualitative in the sense that the model correctly predicts the stresses at which deviations from linear elastic behavior occur as well as the direction of the deviation of the strain from linear behavior.

For comparison with the model, the intergranular strains shown on stereographs in Figures 7(b) and (c) are collapsed and plotted as a function of the azimuthal angle between the reflection and the basal pole in Figure 11. Again, the agreement between the experiment and model is qualitative. The model reproduces the functional form of the intergranular strains, for example, the maximum parallel to the compressive axis, but, in general, underpredicts the magnitude of intergranular strain significantly.

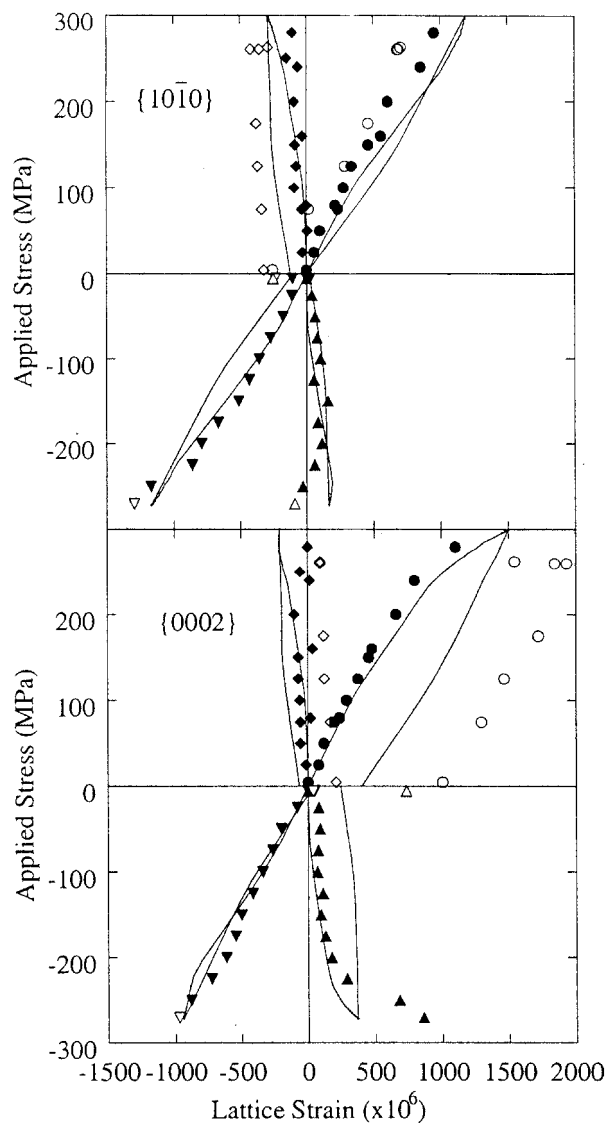


Fig. 10—Experimental and calculated (solid curves) lattice response of  $\{10\bar{1}0\}$  and  $\{0002\}$  reflections to applied tension and compression. ●'s (▲'s) and ◆'s (▼'s) represent the parallel and perpendicular lattice strains in tension (compression) on loading (closed symbols) and unloading (open symbols).

Model calculations were also completed with only basal and prismatic slip active. As stated previously, the thermal residual stress has no resolved component on either the basal or prismatic systems and the calculation necessarily produces identical results (with a sign reversal) in tension and compression. Thus, basal and prismatic activity alone cannot reproduce the asymmetry observed in the tensile and compressive intergranular strains and are insufficient to describe the data even qualitatively.

The possible sources of the underpredicted intergranular strains have to do with assumptions intrinsic to the model, and point toward areas where model improvements can be introduced. To start with, the EPSC model, as proposed by Hill<sup>[12]</sup> and implemented here in a fully anisotropic version, is based on regarding each grain as an elasto-plastic inclusion interacting with an elasto-plastic effective medium. In addition, the stress and strain are regarded as

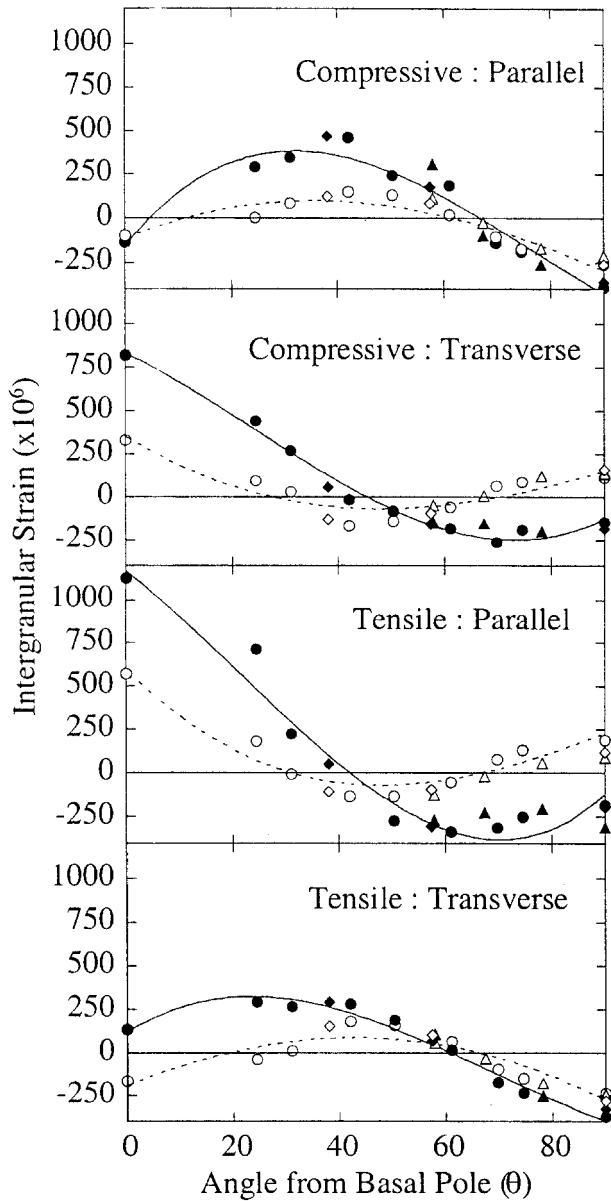


Fig. 11—Experimental (solid symbols) and calculated (open symbols) plasticity-induced intergranular strains at maximum values of macroscopic compressive and tensile strain. ●'s, ▲'s, and ◆'s represent  $hkil$ 's within the planes defined by the {0002} and {10 $\bar{1}$ 0} plane normals, the {0002} and {1120} plane normals, and the {0002} and {12 $\bar{3}$ 0} plane normals, respectively.

homogeneous inside the domain of the inclusion. The deviations in stress and strain between the inclusion and the average medium are controlled by the stiffness of the interaction between the inclusion and the medium: the stiffer the interaction, the smaller the deviations and the closer to an isostrain model. Molinari *et al.*<sup>[37]</sup> convincingly argue that the Hill, approach represents a “secant” approximation, which is on the “stiff” side. As a consequence, increased variations in strain can be expected from grain to grain if the stiffness of the interaction is somewhat relaxed. Such relaxation could be enforced empirically, and we are in the process of investigating this option.

The other assumption of the inclusion formalism is the uniformity of strain within the grain. As a consequence,

the model only captures intergranular strains (type II), but does not describe intragranular strains (type III) that may arise from microstructural features within the grain. In the particular case of beryllium studied here, and judging from the TEM evidence,<sup>[1,24]</sup> pyramidal slip seems to take place in the vicinity of the grain boundary. As a consequence, one may envisage the interior of the grain as a second phase where only basal and prism slip can operate, and the capacity of relieving stresses is reduced. As a consequence, larger strains would result in the interior of the grain and these would weight the diffraction results.

The asymmetry in the development of the plasticity induced intergranular strains under compression or tension is clear, but cannot be reproduced in the model with basal and prismatic slip alone. In addition, the observed intergranular strain in grains with {0002} poles parallel to the compressive axis is relatively small and negative. Because basal and prismatic slip do not permit plastic deformation parallel to the basal pole, the omission of pyramidal slip from the model would result in an overestimation the {0002} intergranular strain in compression by more than 600  $\mu\epsilon$ .

## VII. SUMMARY

*In-situ* neutron diffraction loading measurements of beryllium in uniaxial tension and compression revealed asymmetric behavior in both the macroscopic stress/strain curve measured with an extensometer and the microscopic lattice ( $hkil$ -specific) curves measured by neutron diffraction. In both measurements, the compressive flow curve deviates from linearity at lower applied stress relative to the tensile flow curve. Correspondingly, significant residual stresses develop earlier during compressive loading than tensile. Finally, the asymmetry is characterized microscopically by differences in the { $hkil$ } dependent intergranular strains that develop during plastic deformation.

An EPSC model including thermal residual stresses and basal, prismatic, and pyramidal slip qualitatively reproduces the asymmetry in lattice strains,  $\epsilon_{hkil}$ , with respect to uniaxial tension and compression in beryllium to 0.8 pct strain. However, in general, the model underpredicts the magnitude of the lattice strains. The calculated intergranular strains associated with the thermal residual stresses were comparable in magnitude to the plasticity-induced intergranular strains produced during deformation. The thermal residual stresses are fundamental in explaining the compression/tension asymmetry of the microscopic response but require the assumption of pyramidal slip. This is controversial, but other mechanisms of inelastic deformation, such as twinning and fracture, could not reproduce the observed lattice response to applied stress. Moreover, using the model in its current form, the early macroscopic yield observed in compression was predicted.

## ACKNOWLEDGMENT

This work was performed under the auspices of the DOE under contract number W-7405-ENG-36. The Manuel Lujan Jr. Neutron Scattering Center is a national user facility funded in part by the U.S. DOE.

## REFERENCES

1. L.E. Murr, C.S. Niou, A.H. Advani, L. Vega, S.W. Stafford *et al.*: *Mater. Sci. Eng. A*, 1991, vol. 151, pp. 179-87.
2. F.F. Lavrentyev, O.P. Salita, V.V. Paley, O.V. Matsiyevskiy, and Y.P. Khimich: *Fiz. Metall. Metalloved.*, 1987, vol. 64(6), pp. 1221-24.
3. D.R. Floyd: *Causes of the Yield-Point Phenomenon in Commercial Beryllium Products*, Rocky Flats Division of Dow Chemical, Golden, CO, 1974.
4. S.H. Gelles and J.H. Peterson: *Characteristics of Commercial Vacuum Hot-Pressed Beryllium*, Lawrence Livermore Lab. Columbus, OH, 1972.
5. I.N. Khristenko, II. Papirov, G.F. Tikhinskiy, and L.A. Korniyenko: *Russ. Metall.*, 1978, vol. 4, pp. 94-98.
6. F. Aldinger: in *Beryllium Science and Technology*, D. Webster and G.J. London, eds., Plenum Press, New York, NY, 1979, pp. 7-107.
7. D. Webster, R.L. Greene, R.W. Lawley, and G.J. London: *Metall. Trans. A*, 1976, vol. 7(6), pp. 851-56.
8. C.N. Tomé, M.R. Daymond, and M.A.M. Bourke: *6th Int. Conf. on Residual Stresses*, The Institute of Materials, Oxford, United Kingdom, 2000, pp. 1349-56.
9. M.R. Daymond, M.A.M. Bourke, and R.B. VonDreele: *J. Appl. Phys.*, 1999, vol. 85(2), pp. 739-47.
10. P. Roschke and E. Mascorro: *J. Eng. Mater. Technol. Trans. ASME*, 1996, vol. 118(2), pp. 207-12.
11. D. Beasley, G.I. Turner, and K.L. Edwards: *J. Mater. Sci.*, 1975, vol. 10(3), pp. 436-42.
12. R. Hill: *J. Mech. Phys. Solids*, 1965, vol. 14, p. 95.
13. J.W. Hutchinson: *Proc. R. Soc London A*, 1970, vol. 319, pp. 247-72.
14. T.M. Holden, C.N. Tomé, and R.A. Holt: *Metall. Trans. A*, 1998, vol. 29(12), pp. 2967-73.
15. B. Clausen, T. Lorentzen, M.A.M. Bourke, and M.R. Daymond: *Mater. Sci. Eng. A*, 1999, vol. 259(1), pp. 17-24.
16. B. Clausen, T. Lorentzen, and T. Leffers: *Acta Mater.*, 1998, vol. 46 (9), pp. 3087-98.
17. J.W.L. Pang, T.M. Holden, J.S. Wright, and T.E. Mason: *Acta Mater.*, 2000, vol. 48(5), pp. 1131-40.
18. J.W.L. Pang, T.M. Holden, and T.E. Mason: *Acta Mater.*, 1998, vol. 46(5), pp. 1503-18.
19. M.R. Daymond, C.N. Tomé, and M.A.M. Bourke: *Acta Mater.*, 2000, vol. 48(2), pp. 553-64.
20. P.A. Turner and C.N. Tomé: *Acta Metall.*, 1994, vol. 42(12), pp. 4143-53.
21. J.W.L. Pang, T.M. Holden, and T.E. Mason: *J. Strain Analysis Eng. Design*, 1998, vol. 33(5), pp. 373-83.
22. S. Jonsson and J. Beuers: *Mater. Sci. Eng.*, 1987, vol. 91, pp. 111-23.
23. G.J. London, V.V. Damiano, and H. Conrad: *Trans. TMS*, 1968, vol. 242, pp. 979-94.
24. R.D. Field, K.T. Hartwig, C.T. Necker, J.F. Bingert, and S.R. Agnew: *Metall. Mater. Trans. A*, 2002, vol. 33A, pp. 965-72.
25. R.W. Armstrong and N.R. Borch: *Metall. Trans.*, 1971, vol. 2, pp.3073-77.
26. D.W. Brown, R. Varma, M.A.M. Bourke, P. Burgardt, S. Spooner *et al.*: *Advances in X-Ray Analysis*, Denver X-ray Conf. 2001, International Center for Diffraction Data, Denver, CO., 2001, vol. 44, pp. 162-67.
27. K. Bennett, R. Varma, and R.B. VonDreele: *Scripta Mater.*, 1999, vol. 40(7), pp. 825-30.
28. J.E. Hanafec: *J. Appl. Met. Working*, 1980, vol. (3), p. 41.
29. M.A.M. Bourke, J.A. Goldstone, and T.M. Holden: in *Measurement of Residual and Applied Stress Using Neutron Diffraction*, M.T. Hutchings and A.D. Krawitz, eds., Kluwer Academic Publishers, Dordrecht, The Netherlands, 1992, pp. 369-82.
30. N. Shi, M.A.M. Bourke, J.A. Roberts, and J.E. Allison: *Metall. Trans. A*, 1997, vol. 28(12), pp. 2741-53.
31. C. Tomé, G.R. Canova, U.F. Kocks, N. Christodoulou, and J.J. Jonas: *Acta Metall.*, 1984, vol. 32(10), pp. 1637-53.
32. N.R. Borch: in *Beryllium Science and Technology*, D. Webster and G.J. London, eds., Plenum Press, New York, NY, 1979, pp. 307-30.
33. S. Jonsson: *Z. Metallkd.*, 1984, vol. 75(7), pp. 523-28.
34. C.N. Tomé, W.R. Blumenthal, M.A.M. Bourke, D.W. Brown, G.C. Kaschner, and P. Rangaswamy: *Proc. of ICOTOM-13, Mats. Sc. Forum* 408-412, 2002, pp. 263-68.
35. D.W. Brown, M.A.M. Bourke, P.S. Dunn, R.D. Field, M.G. Stout, and D.J. Thoma: *Metall. Trans. A*, 2001, vol. 32, pp. 2219-28.
36. S.R. Macewen, C. Tomé, and J. Faber: *Acta Metall.*, 1989, vol. 37(3), pp. 979-89.
37. A. Molinari, S. Ahzi, and R. Kouddane: *Mech. Mater.*, 1997, vol. 26(1), pp. 43-62.